

# Statistics of time and frequency-averaged spectra in gravitational-wave background searches

Quentin Baghi

*Université Paris Cité, CNRS, Astroparticule et Cosmologie, F-75013 Paris, France*

Nikolaos Karnesis

*Department of Physics, Aristotle University of Thessaloniki  
Thessaloniki 54124, Greece*

Jean-Baptiste Bayle

*IRFU, CEA, Université Paris-Saclay, F-91191 Gif-sur-Yvette, France*

(Dated: February 16, 2026)

Time series analysis from gravitational-wave detectors often relies on the assumption that time chunks, or frequency bins, are uncorrelated. We discuss the validity of this approximation in the context of searches for stochastic gravitational-wave backgrounds. We examine the impact of averaging over time and frequency, a reduction technique commonly employed to minimize the computational expense of likelihood evaluations. We introduce an analytical tool based on Fisher information to quantify the error in parameter inference arising from ignoring these effects. Finally, we address the issue of locally stationary processes and optimal time chunking.

## I. INTRODUCTION

Searching for stochastic signals in gravitational wave (GW) detector data is a delicate task, as the signal shares common characteristics with the instrumental noise [1, 2]. They can usually be described by random processes exhibiting some degree of stationarity and Gaussianity, as well as continuous spectra. Additionally, stochastic gravitational-wave background (SGWB) searches require the analysis of long time series on a wide frequency range to make faint signals emerge, which requires a large volume of raw data. To reduce the computational cost of such an analysis, it is necessary to choose a representation in which the noise covariance is sparse; this is typically achieved in the Fourier domain or using some time-frequency basis functions. To further reduce the cost, a practical approach is to bin the data, i.e., chunk it in time or frequency and average spectral estimates. This is a common practice in spectral analysis, particularly in ground-based detector searches. The periodograms may be computed on many segments and then stacked [3, 4], keeping each segment long enough to explore the lower end of the band. This estimation method is referred to as weighted overlapped segment averaging (WOSA) [5] or Welch's spectral estimation [6].

While it is used in analyses requiring time chunking, the data compression obtained by averaging periodograms of time segments is limited by the lowest frequency of the band of interest. An alternative is to smooth spectral ordinates in the frequency domain; for example, by applying a moving average. This method has been used to reduce the frequency resolution in LIGO–Virgo analyses (e.g., [7]) and in some recent studies relative to the future Laser Interferometer Space Antenna (LISA) mission [8–12].

Nevertheless, transforming data from the time domain

to the frequency domain comes with spectral artifacts, which reflect in any subsequent averaging. Any finite windowing (or tapering) leads to spectral leakage and correlations among frequency bins. These correlations affect the statistics of spectral estimates constructed from averaging periodograms. In Welch's approach, correlations of nearby segments decrease the effective number of averaged segments. In smoothing spectral estimates, a similar effect occurs from correlations between nearby frequency bins. Although sometimes mentioned [13], these effects are not always accounted for in SGWB searches, with some exceptions like in [14], where the authors account for the windowing in the Welch's periodogram statistics.

Spectral correlations have recently aroused interest in the GW community. Sala and Vitale [15] have proposed a Bayesian approach to multivariate spectral estimation, although considering frequency bins as independent. In the context of Advanced LIGO/Virgo, Talbot *et al.* [16] have recently investigated the effect of windowing and demonstrated that they can lead to errors in compact binary inference which are comparable to other known systematic effects like calibration errors. This type of investigation is also relevant to LISA data analysis. While many studies in this context have been based on data directly simulated in the frequency domain, as LISA has passed the “adoption” milestone [17], the tendency is to move towards more realistic assumptions and time-domain simulations. This is particularly the case of the works that consider the search for anisotropic SGWBs for their analysis, like Adams and Cornish [18], Boileau *et al.* [19, 20], Hindmarsh *et al.* [14], Criswell *et al.* [21, 22], Buscicchio *et al.* [12, 23], Pozzoli *et al.* [24]. Besides, Burke *et al.* [25] have shown that the structure of the discrete Fourier transform (DFT) covariance can significantly deviate from the diagonal assumption

in the presence of data gaps, depending on the assumptions about the LISA noise power spectrum. Cornish [26] has also investigated the conditions for having a diagonal covariance in time-frequency representations like wavelet packet bases. Even without interruptions, finite duration effects will likely have a significant impact on LISA data analysis, given the level of expected signal-to-noise ratios (SNRs) for some GW sources. Note that analyses of pulsar timing arrays differ, as they are usually performed directly in the time domain, by modeling the unevenly sampled times of arrivals using Gaussian processes (see, for example, [27]).

The primary objective of this publication is to compile a fundamental analytical description of correlation effects in the context of power spectral density estimation, and to provide tools for assessing these effects. Our focus is specifically on the interplay between correlations and binning techniques used for data reduction. We apply our tools to searches for SGWBs with LISA. We demonstrate that, if not accounted for, these effects can lead to an incorrect assessment of the uncertainty of astrophysical or cosmological parameters when performing inference on SGWBs signals.

The second goal of this work is to assess the error related to the smoothing of spectral estimates and to construct reliable estimators. Smoothing may indeed lead to bias, as this technique assumes that the underlying power spectral density (PSD) is approximately constant on short frequency bandwidths, and can therefore be coarse-grained. A bias in estimating the spectrum typically translates into a bias in parameters when doing inference. To evaluate this bias, we propose an analytical tool based on the Fisher information matrix, which applies the rationale developed in [28] to spectral templates instead of waveforms. The tool allows one to find the optimal trade-off between parameter accuracy and spectral data compression, a manifestation of the infamous bias-variance trade-off.

We start in Sec. II by reviewing standard definitions and results describing the covariance of stationary time series. Then, in Sec. III, we discuss the effect of correlations on time-averaged spectral estimates (Welch's method), and in Sec. IV we consider the impact of frequency correlations on spectral smoothing. In Sec. V, we explore the implications on spectral parameter estimation by deriving an estimate of the bias whenever using an incorrect spectrum template. We generalize this framework to multivariate time series and locally stationary processes. In Sec. VII we apply this formalism to a numerical experiment simulating a SGWB search in LISA data. We finally discuss our results in Sec. IX.

## II. COVARIANCE OF STATIONARY TIME SERIES

### A. Time and frequency-domain covariances

We consider a time series  $\mathbf{x}$  of size  $N$  described by a zero-mean, Gaussian, weak-sense stationary process of covariance  $\Sigma_{xx}$ . We assume it is sampled at a frequency  $f_s$  (equivalent to a sampling time  $\tau_s$ ). Hence, its duration is  $T = N\tau_s$ . Weak-sense stationarity implies that the covariance of two samples only depends on the duration separating them. Formally, this means that there exists an autocovariance function  $R_{xx}(t)$  such that

$$\Sigma_{xx}(i, j) = R_{xx}((j - i)\tau_s), \quad \forall i, j \in [0, N]. \quad (1)$$

The autocovariance function is related to the one-sided PSD function  $S_{xx}(f)$  through an inverse Fourier transform:

$$R_{xx}(t) = \frac{1}{2} \int_{-\frac{f_s}{2}}^{+\frac{f_s}{2}} S_{xx}(f) e^{2i\pi f t} df. \quad (2)$$

Most of the analysis in gravitational-wave science is done in the Fourier domain. We define the windowed DFT of any time series  $\mathbf{x}$  with the following convention:

$$\tilde{x}_N(f_k) = \tau_s \sum_{n=0}^{N-1} w_n x_n e^{-2i\pi \frac{nk}{N}}. \quad (3)$$

which has the same dimension as the continuous Fourier transform. In this definition, the index  $k$  corresponds to frequency  $f_k = k/T$  if  $k \leq \lfloor \frac{N-1}{2} \rfloor$  and  $f_k = (k - N)/T$  if  $k > \lfloor \frac{N-1}{2} \rfloor$ . The definition includes a taper window  $\mathbf{w}$  to prevent leakage effects. However, the classical DFT assumes  $w_n = 1$  for all  $n$ .

Let us consider the structure of the covariance matrix in the frequency domain  $\tilde{\Sigma}$ . One can show that its elements are

$$\begin{aligned} \tilde{\Sigma}_N(k, l) &= \mathbb{E}[\tilde{x}_N(f_k) \tilde{x}_N^*(f_l)] \\ &= \frac{1}{2} \int_{-\frac{f_s}{2}}^{+\frac{f_s}{2}} \tilde{w}_N(f_k - f) \tilde{w}_N^*(f_l - f) S_{xx}(f) df. \end{aligned} \quad (4)$$

This expression encodes two effects arising when considering finite, windowed time series: i) power leakage and ii) correlations of neighboring frequency bins. The first effect induces a distortion of the theoretical PSD in the diagonal elements of the covariance. This is due to the convolution with the squared modulus of the window's DFT, which deviates from a Dirac function for finite  $N$  and exhibits side lobes. The second effect results in non-zero off-diagonal terms in the frequency-domain covariance, arising from the width of main lobe of  $\tilde{w}_N(f)$ . Usually, windows tailored to reduce leakage tend to increase inter-bin correlations.

If all window points are non-zero, then the windowed DFT follows a complex Gaussian distribution whose probability density function (PDF) is given by Eq. (34). However, most tapering windows precisely smoothly drop to zero at the edges of the time series. The consequence is that the matrix  $\tilde{\Sigma}$  is singular (see [16, 25]). Indeed, windowing amounts to multiplying the time-domain covariance matrix on both sides by a diagonal matrix whose diagonal elements  $(n, n)$  are equal to  $w_n$ . Therefore, the determinant of the resulting matrix is null. As an inverse covariance is required to compute the likelihood, one can resort to a regularisation through truncated singular value decomposition (SVD).

## B. Spectrum estimation with the periodogram

In SGWB searches, basic spectrum estimation rely on the windowed periodogram that we define as

$$P_N(f_k) \equiv \frac{2}{\tau_s \kappa_N} |\tilde{x}_N(f_k)|^2. \quad (5)$$

This definition is consistent with a one-sided PSD. Hence, the expectation of the windowed periodogram over infinite noise realizations is approximately given by  $S(f_k)$ , if one ignores frequency leakage:

$$\mathbb{E}[P_N(f_k)] \approx S(f_k). \quad (6)$$

Finite-size windowing induces deviations from this approximation, as mentioned later in Sec. II A. When  $N$  tends to infinity, this quantity is approximately proportional to a chi-squared distribution:

$$P_N(f_k) \approx \begin{cases} \frac{1}{2} S(f_k) \chi_2^2 & \text{for } 0 < |f_k| < \frac{f_s}{2} \\ S(f_k) \chi_1^2 & \text{for } |f_k| = 0 \text{ or } |f_k| = \frac{f_s}{2}. \end{cases} \quad (7)$$

SGWB searches require using long observations to accumulate SNR. A direct analysis of the frequency-domain data is computationally expensive as  $N$  gets large. Instead, many authors use binning, i.e., averaging periodograms obtained from contiguous data segments, or direct averaging in the frequency domain. We explore the implications of this strategy in the following.

## III. EFFECT OF BINNING IN THE TIME DOMAIN

We refer to the process of averaging spectral estimates in the time or frequency domain as ‘binning’. Binning reduces both the variance of spectral estimates and the computational cost of the likelihood. However, it usually modifies the periodogram distribution and thereby the likelihood. In this section, we investigate the effect of averaging periodograms of several time segments, also called Welch’s method [6], on the likelihood function.

### A. Mean and variance of spectral estimates

Welch’s method consists of partitioning the time series into  $M$  segments of length  $L$  that are potentially overlapping, and averaging their periodograms. Similarly to Eq. (3), we can define the (tapered) DFT of the  $m^{\text{th}}$  segment  $\forall m \in [0; M-1]$ :

$$\tilde{x}^m(f_k) = \tau_s \sum_{n=0}^{L-1} w_n x_{(n+ms)} e^{-2i\pi \frac{nk}{N}}, \quad (8)$$

where  $s \in ]0; L]$  is the shift in samples between two consecutive segments. By defining  $p = (L-s)/N$  as the percentage of overlap between two consecutive segments, we have the following relationship between  $M$ ,  $L$  and  $p$  [29]:

$$ML(1-p) + Lp = N. \quad (9)$$

Welch’s PSD estimator computes the average of the segment periodograms as

$$\bar{P}_L(f_k) = \frac{1}{M} \sum_{m=0}^{M-1} P_L^m(f_k), \quad (10)$$

where  $P_L^m(f_k)$  is the periodogram of segment  $L$  evaluated at frequency  $f_k$ :

$$P_L^m(f_k) \equiv \frac{2}{\tau_s \kappa_L} |\tilde{x}^m(f_k)|^2. \quad (11)$$

The expectation of the Welch’s periodogram is equal to the diagonal element of the frequency-domain covariance of a segment of length  $L$ , as introduced in Eq (4):

$$\begin{aligned} \mathbb{E}[\bar{P}_L(f_k)] &= \frac{2}{\tau_s \kappa_L} \tilde{\Sigma}_L(k, k) \\ &= \frac{1}{\tau_s \kappa_L} \int_{-\frac{f_s}{2}}^{+\frac{f_s}{2}} |\tilde{w}_L(f_k - f)|^2 S_{xx}(f) df. \end{aligned} \quad (12)$$

For convenience, we will denote this expectation by

$$\bar{S}_L(f_k) \equiv \mathbb{E}[\bar{P}_L(f_k)] \quad (13)$$

in the following. When the windowing is adapted, and  $L$  is sufficiently large, it can be approximated by the true PSD  $\bar{S}_L(f_k) \approx S(f_k)$ .

To compute the variance, one has to account for cross-covariances between segment periodograms. We have [29]:

$$\text{Var}[\bar{P}_L(f_k)] \approx \frac{\text{Var}[P_L(f_k)]}{M} \left( 1 + \frac{2}{M} \sum_{m < m'}^{M-1} c_{mm'}(f_k) \right) \quad (14)$$

where  $c_{mm'}$  is the correlation coefficient of two segment periodograms:

$$c_{mm'}(f_k) \equiv \frac{\text{Cov}[P_L^m(f_k), P_L^{m'}(f_k)]}{\sqrt{\text{Var}[P_L^m(f_k)] \text{Var}[P_L^{m'}(f_k)]}}. \quad (15)$$

Note that  $\text{Var}[P_L^m(f_k)] = \text{Var}[P_L^{m'}(f_k)] \approx \bar{S}_L(f_k)^2$  for all  $m$  (the segment periodograms have all the same variance, approximately equal to their squared expectation). From Eq. (14) we see that the variance of the averaged segment periodograms is not simply the variance of a single periodogram divided by  $M$ . Due to correlations among segment periodograms  $P_L^m(f_k)$ , there is a penalizing term that increases it. Consequently, in general, Welch's estimate does not simply follow a chi-squared distribution with  $2M$  degrees of freedom (DOFs) as it would if segments were uncorrelated. Rather, the statistical distribution of  $\bar{P}_L(f_k)$  can be approximated to be proportional to a chi-squared distribution with an effective number of DOFs  $\nu < M$  that accounts for segment-to-segment correlations [30]:

$$\bar{P}_L(f_k) \sim a \chi_{\nu}^2. \quad (16)$$

In order for this distribution to have the same mean and variance, we require  $\nu$  to be [31]

$$\nu = \frac{2\bar{S}_L(f_k)^2}{\text{Var}[\bar{P}_L(f_k)]}, \quad (17)$$

and  $a$  to be

$$a = \frac{\bar{S}_L(f_k)}{\nu}. \quad (18)$$

Plugging Eq. (14) into Eq. (17), one gets

$$\nu \approx \frac{2M}{1 + \frac{2}{M} \sum_{m < m'}^{M-1} c_{mm'}(f_k)}. \quad (19)$$

As shown in Sec. B, the correlation coefficients mainly depend on the window, and can be approximated as

$$c_{mm'}(f_k) \approx \frac{1}{\kappa_L^2} \left| \sum_{n=0}^{L-1} w_n w_{n+s|(m'-m)|} \right|^2, \quad (20)$$

which greatly simplify the computation of the sum in Eq. (19).

We verify that if we ignore correlations ( $c_{mm'} = 0$  for  $m \neq m'$ ), then the effective number of DOFs reduces to  $2M$ . Note that assuming the averaged periodogram is proportional to a chi-squared random variable is equivalent to assuming that it follows a gamma distribution. This modeling approach is adopted and justified in [32] in the context of massive black hole detection with LISA.

## B. Example using simulated samples

We illustrate the effect of correlations in time binning with a numerical experiment. We consider a time series generated from a PSD  $S_{xx}$  describing the instrumental noise in the second-generation Michelson time-delay interferometry (TDI)  $X$  in the LISA space mission (see, e.g., [33] for a definition). The analytical expression for

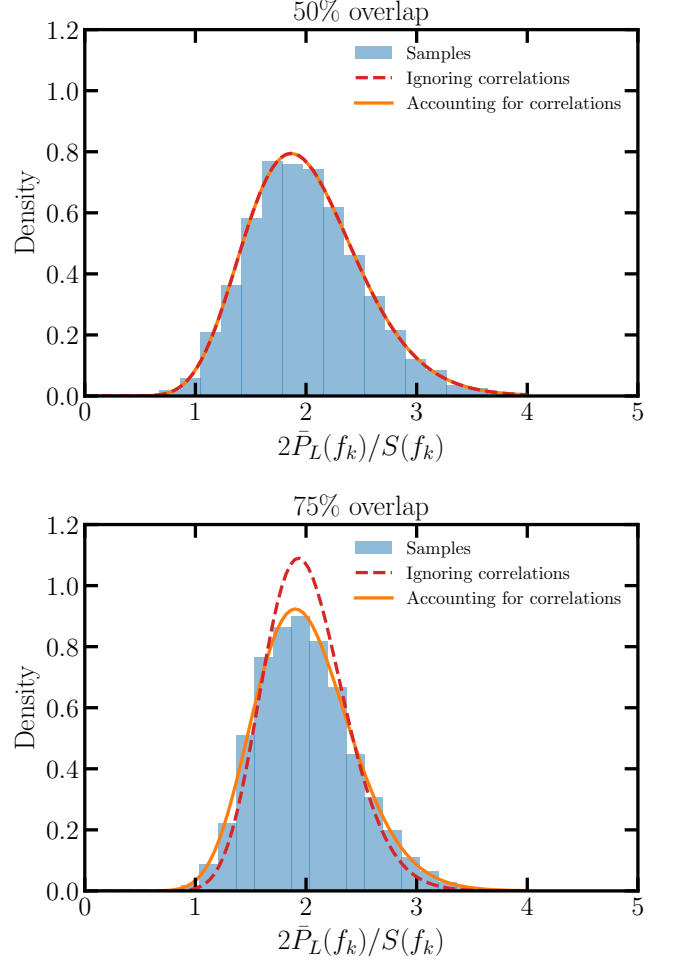


FIG. 1. Blue histograms: Welch's periodogram distribution using  $10^4$  realizations of the same noise PSD at  $f = 1\text{ mHz}$  with segment overlaps of  $p = 50\%$  (upper panel)  $p = 75\%$  (lower panel). Lines: distributions modeled with Eq. (16) with  $2M$  DOFs (dashed red) and  $\nu$  DOFs (solid orange). Segment correlations start contributing with overlaps larger than 50 %, and ignoring correlations leads to underestimating the variance.

the PSD function is given in Sec. A. We choose  $N = 8192$ ,  $f_s = 6 \times 10^{-2}$  Hz, and generate  $10^4$  realizations of the noise process.

For all realizations, we compute Welch's periodogram with a segment size of  $L = 1024$  and a Blackman-Harris window using two percentages of overlap  $p = 0.5$  and  $p = 0.75$ . We plot the distribution of the periodogram evaluated at a single frequency  $f = 1$  mHz in Fig. 1 for the two choices of overlaps.

In the case of 50 % overlap (top panel), which corresponds to the separation between two maxima of the window, the distribution (orange) is indistinguishable from a chi-squared distribution with  $2M$  degrees of freedom (dashed red), as we would have for perfectly uncorrelated periodograms. Increasing the overlap to 75% (lower panel) breaks this approximation, and the distribution

that ignores correlations significantly deviates from the one with an adjusted number of DOFs.

One advantage of the Welch's method is that it reduces the frequency resolution to lower the computational cost of any spectral inference, without introducing a bias other than spectral leakage. However, the computational gain is moderate. If one considers a stochastic background concentrated on a bandwidth  $B = f_{\max} - f_{\min}$ , the number of relevant frequency bins is  $N_f = BL\tau_s$ . The lower frequency bound sets the minimum of the segment lengths:  $L_{\min} = 1/(\tau_s f_{\min})$ . Therefore, the best reduction of the number of points one can get is  $r = N/L_{\min} = \tau_s f_{\min}$ . This is why it may be interesting to use smoothed spectrum estimates in the frequency domain, as described in the next section.

#### IV. EFFECT OF BINNING IN THE FREQUENCY DOMAIN

Another way of compressing the data is to compute the periodogram of the full time series and average its frequency bins. The simplest way is to split the Fourier band into  $J$  segments. Each segment has size  $N_j$  and is centered around a frequency  $f_j$ . We can then average all the periodogram bins inside each segment as

$$\bar{P}_N(f_j) \equiv \frac{1}{N_j} \sum_{k=j-K_j}^{j+K_j} P_N(f_k), \quad (21)$$

where we took odd segment sizes  $N_j = 2K_j + 1$  to get the same number of frequency bins below and above the central frequency. Note that for the sake of generality, we allow the number of averaged Fourier frequencies to depend on the segment index  $j$ . In the following, we discuss the consequences of frequency-domain averaging on spectral precision and accuracy.

##### A. Mean and variance of spectral estimates

We aim at studying the statistics of  $\bar{P}_N$ . Let us first consider its mean:

$$\mathbb{E}[\bar{P}_N(f_j)] = \frac{1}{2K_j + 1} \sum_{k=j-K_j}^{j+K_j} \bar{S}_N(f_k), \quad (22)$$

where  $\bar{S}_N(f_k) = \mathbb{E}[\bar{P}_N(f_k)]$  is the expectation of the periodogram bins which is directly proportional to the diagonal elements of the frequency-domain covariance in Eq. (4). In general, the power leakage may result in distortions of the PSD. However, we assume that the window  $w$  is well chosen so that they are negligible. We can write  $\bar{S}_N(f_k) \approx S(f_k)$ . If we Taylor-expand the PSD around the central frequency  $f_j$  of the segment, we find

$$\mathbb{E}[\bar{P}_N(f_j)] \approx S(f_j) + \frac{1}{2N_j} \sum_{k=j-K_j}^{j+K_j} S''(f_j)(f_k - f_j)^2, \quad (23)$$

where  $S''$  refers to the second derivative of the PSD. The first-order terms do not appear as they average out in the sum.

As each periodogram bin  $P_N(f_k)$  is proportional to a chi-squared distribution with two degrees of freedom, if they were uncorrelated, their average would be proportional to a chi-squared distribution with  $2N_j$  degrees of freedom. More precisely, we would have  $2\bar{P}_{xx}(f_j)/S(f_j) \sim \chi^2_{2N_j}$ , assuming the PSD is constant over the entire segment.

However, we saw in Sec. II A that different frequency bins are usually correlated over a certain bandwidth depending on the window. We can proceed similarly as for the time averaging: we postulate that  $\bar{P}_N(f_j)$  is proportional to a random variable following a chi-squared distribution with some DOFs to be determined, as in Eq. (16).

We can compute the effective number of DOFs from the ratio between the expectation and the variance of the averaged periodogram, as in Eq. (17). The expression for the variance has the same form as in Eq. (14):

$$\text{Var}[\bar{P}_N(f_j)] \approx \frac{\text{Var}[P_N(f_j)]}{N_j} \left( 1 + \frac{2}{N_j} \sum_{\substack{k < k' \\ j - K_j}}^{j+K_j} \sigma_{kk'} \right), \quad (24)$$

where  $\sigma_{kk'}$  is the periodogram correlation coefficient among different frequencies:

$$\sigma_{kk'} \equiv \frac{\text{Cov}[P_N(f_k), P_N(f_{k'})]}{\sqrt{\text{Var}[P_N(f_k)] \text{Var}[P_N(f_{k'})]}}. \quad (25)$$

We obtain an expression for the effective number of DOFs that is similar to the one we got in Eq. (B10) for time-averaged periodograms:

$$\nu(f_j) = \frac{2N_j}{\left( 1 + \frac{2}{N_j} \sum_{k < k'} \sigma_{kk'} \right)}. \quad (26)$$

Similarly to the correlations of the different segment periodograms, the correlations among the different frequencies depend only on the window at first order:

$$\sigma_{kk'} \approx \frac{1}{\kappa_N^2} \left| \sum_{n=0}^{N-1} w_n^2 e^{-\frac{2i\pi(k-k')}{N}} \right|^2. \quad (27)$$

We derive this result in Sec. C.

##### B. Example on simulated samples

As for time averaging, we illustrate the effect of correlations in frequency binning with a numerical experiment. We consider the same simulation set as in Sec. III B, with the same number of realizations.

We choose a frequency segment of size  $N_j = 11$  centered around  $f_j = 1$  mHz. For each realization, we compute the averaged periodogram following Eq. (21),

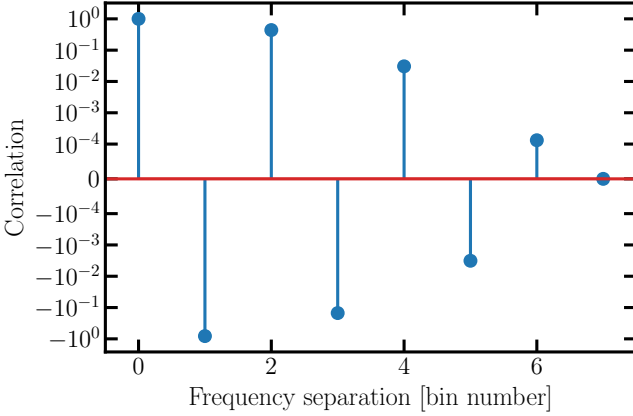


FIG. 2. Values of the first row of matrix  $\mathbf{C}$  as a function of the frequency separation (in number of bins). The  $y$  axis is displayed on a symmetric logarithmic scale centered around zero.

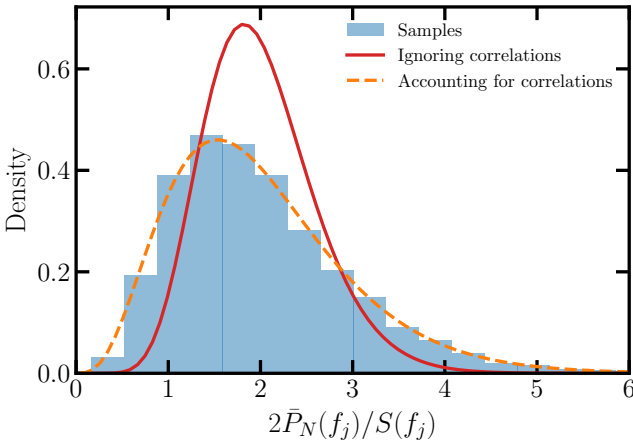


FIG. 3. Averaged periodogram distribution using  $10^4$  realizations of the same noise PSD for  $f_j = 1$  mHz.

using a Blackman-Harris window, and the quantity  $2\bar{P}_{xx}(f_j)/S_{xx}(f_j)$ . We obtain the histogram in Fig. 3 (in light blue). Naively trying to describe the distribution with a chi-squared PDF with  $2N_j$  degrees of freedom leads to the red solid curve. We observe that this modelling is not accurate, largely overestimating the width of the distribution.

Then, we compute the theoretical correlation coefficients  $\sigma_{kk'}$ . For a fixed frequency bin  $k$ , we plot it as a function of the frequency bin separation in Fig. 2. The correlation is significant for bin separations of 1 and 2, and then drops below  $10^{-3}$  quickly. Therefore, one could approximate the correlation matrix by a banded matrix with a few non-zero diagonals.

We compute the chi-squared distribution in Eq. (16) using the effective number of DOFs computed with Eq. (26). We obtain the dashed orange curve in Fig. 3, which better agrees with the empirical distribution. The

ratio between the variance of the two chi-squared distributions is about  $\nu/2N_j \sim 20\%$ . Therefore, ignoring bin-to-bin correlations in this case would result in the uncertainties of inferred astrophysical or cosmological parameters being underestimated by 80%.

### C. Bias-variance trade-off

Using Eq. (21) to average periodogram bins in the frequency domain decreases the variance of spectral estimates while increasing the bias. The segment size  $N_j$  controls this trade-off. Therefore, looking for the best data compression requires finding the maximum value of  $N_j$  for which the bias remains low enough.

#### 1. For spectral estimates

If one is interested in computing accurate spectral estimates with the minimal variance, the root mean squared error (RMSE)  $\epsilon$  is a possible figure of merit. Let us consider a frequency bandwidth  $B = f_{\max} - f_{\min}$ . We define the RMSE over  $B$  as

$$\epsilon^2 = \frac{1}{N_B} \sum_{j=j_{\min}}^{j_{\max}} (\bar{P}_N(f_j) - S(f_j))^2, \quad (28)$$

where we choose the lower bound of the first frequency segment (respectively the upper bound of the last segment) to coincide with the bandwidth's lower bound (respectively upper bound):  $f_{\min} = f_{j_{\min}} - K_j/T$ ;  $f_{\max} = f_{j_{\max}} + K_j/T$ . We also set the number of frequency bins in the bandwidth  $N_B = j_{\max} - j_{\min} + 1$ . Rather than the RMSE, which depends on the realization of the stochastic process, we consider the statistical expectation of  $\epsilon^2$ :

$$\begin{aligned} \mathbb{E}[\epsilon^2] &= \frac{1}{N_B} \sum_{j=j_{\min}}^{j_{\max}} \text{Var}[\bar{P}_N(f_j)] + \text{Bias}^2[\bar{P}_N(f_j)], \\ &= \sigma^2 + b^2 \end{aligned} \quad (29)$$

where the variance of the averaged spectra is approximately

$$\text{Var}[\bar{P}_N(f_j)] \approx \frac{2}{\nu(f_j)} S(f_j)^2, \quad (30)$$

and we defined the bias as

$$\text{Bias}[\bar{P}_N(f_j)] \equiv \mathbb{E}[\bar{P}_N(f_j)] - S(f_j). \quad (31)$$

The quantities  $\sigma^2 + b^2$  are just the contributions of the total variance and of the total bias to the RMSE, respectively. From Eq. (23), one can evaluate the bias as a function of the second derivatives of the PSD:

$$\begin{aligned} \text{Bias}[\bar{P}_N(f_j)] &\approx \frac{1}{2N_j} \sum_{k=j-K_j}^{j+K_j} S''(f_j)(f_k - f_j)^2 \\ &= S''(f_j) \frac{K_j(K_j + 1)}{6T^2}, \end{aligned} \quad (32)$$

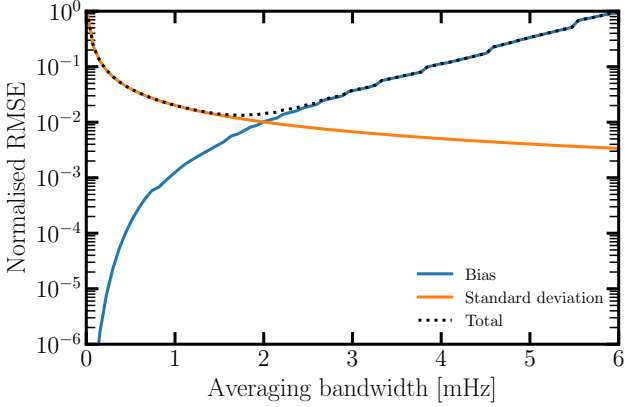


FIG. 4. Expected bias and variance of smoothed spectral estimates (normalized by the PSD) as a function of the averaging bandwidth, for an observation time of about  $1.4 \times 10^5$  seconds.

where in the last line we used the analytical formula for the sum of squared integers. As expected, the larger the PSD second derivative, the larger the bias. It also increases with the square of the averaging bandwidth  $K_j/T$ .

To find an optimal trade-off between bias and variance, one can compute the total bias  $b$  and the total standard deviation  $\sigma$  normalized by the PSD as a function of the averaging bandwidth. We present the results in Fig. 4 for the same case study as previously. The plot indicates that the crossing point is located around 2 mHz. This means that above this bandwidth, the bias is significant compared to the periodogram variance. This computation offers a simple tool to tune smoothing in spectrum estimation, provided that an estimate of the PSD is available.

However, when inferring parameters controlling the PSD, this type of assessment may not be accurate enough. In particular, if some parameters influence different frequency regions or faint features in the spectrum, the global trade-off provided by Fig. 4 may underestimate the maximum averaging one can do without introducing a significant bias in parameter estimates. We address this issue in the following section.

## V. BIAS AND VARIANCE IN PARAMETER INFERENCE

So far, we have studied the effect of averaging on spectral estimates themselves. In this section, we extend the study to the case where the PSD depends on unknown parameters that must be estimated.

### A. Gaussian stationary likelihood

Performing parameter estimation requires to write down a likelihood function. Under the assumptions

stated in Sec. II, we can write the PDF of the time series  $\mathbf{x}$  as

$$f_{\mathbf{x}}(\mathbf{x}) = \frac{\exp\left(-\frac{1}{2}\mathbf{x}^T \Sigma^{-1} \mathbf{x}\right)}{\sqrt{(2\pi)^N |\Sigma|}}. \quad (33)$$

For now, let us assume that  $w_n \neq 0 \ \forall n$ . Then, the windowed DFT vector  $\tilde{\mathbf{x}}_N$  of entries  $\tilde{x}_N(f_k)$  follows a zero-mean complex Gaussian distribution:

$$f_{\tilde{\mathbf{x}}_N}(\tilde{\mathbf{x}}_N) = \frac{\exp\left(-\tilde{\mathbf{x}}_N^\dagger \tilde{\Sigma}_N^{-1} \tilde{\mathbf{x}}_N\right)}{\pi^N |\tilde{\Sigma}_N|}, \quad (34)$$

where  $\tilde{\Sigma}_N$  is the covariance of  $\tilde{\mathbf{x}}_N$ . One can show that  $\tilde{\Sigma}_w$  is a Toeplitz matrix, which means it has constant diagonals.

### B. Whittle's approximation of the likelihood

Whittle's approximation consists of ignoring the exact structure of the covariance and assumes that  $\Sigma_N$  is circulant, which is achieved when  $N$  tends to infinity. Following this assumption, the frequency-domain covariance is approximately diagonal:

$$\tilde{\Sigma}_N \approx \text{diag}(\Delta), \quad (35)$$

and the diagonal elements  $\Delta$  are proportional to the PSD, so that

$$\Delta(k) = \frac{\kappa_N \tau_s}{2} S(f_k). \quad (36)$$

Therefore, Whittle's approximation has two aspects: by ignoring windowing effects, it disregards correlations among frequency bins (i.e., the off-diagonal terms of the covariance matrix) and the effects of leakage on neighboring frequencies (i.e., diagonal term distortions). Note, however, that leakage may be accounted for while preserving the same likelihood form [29, 34]. Eq. (34) is approximated by

$$f_{\tilde{\mathbf{x}}_N}(\tilde{\mathbf{x}}_N) \approx \frac{\exp\left(-\sum_{k=0}^{N-1} \frac{|\tilde{x}_N(f_k)|^2}{\Delta(k)}\right)}{\pi^N \prod_{k=0}^{N-1} \Delta(k)}. \quad (37)$$

We call this PDF Whittle's likelihood. When taking the logarithm, it takes the well-known form

$$\log f_{\tilde{\mathbf{x}}_w} = - \sum_{k=0}^{N-1} \left[ \frac{|\tilde{x}_N(f_k)|^2}{\Delta(k)} + \log \Delta(k) \right] \quad (38)$$

where we ignored the constant terms.

### C. Whittle's likelihood with binned data

We saw that binning modifies the expectation-to-variance ratio of the distribution, which is directly related to the effective number of DOFs. Let us call  $\bar{P}$  a

spectral estimate obtained by averaging, either in time (Welch's method) or in frequency (spectral smoothing). From the approximation in Eq. (16), one can derive the log-likelihood of averaged spectral estimates:

$$\log f_{\bar{P}} = - \sum_{j=j_{\min}}^{j_{\max}} \frac{\nu_j}{2} \left[ \frac{\bar{P}(f_j)}{\bar{S}(f_j)} + \log \bar{S}(f_j) \right], \quad (39)$$

where we dropped the constant terms and used  $\bar{S} = \mathbb{E}[\bar{P}]$ . We also restricted the analysis to some bandwidth set by  $j_{\min}$  and  $j_{\max}$ . In the case of time averaging,  $\bar{P}$  is the Welch's periodogram  $\bar{P}_L$  and  $\nu_j$  is the effective number of DOF computed by Eq. (B10). In the case of frequency averaging,  $\bar{P}$  is the smoothed periodogram  $\bar{P}_N$  and  $\nu_j$  is the effective number of DOF provided by Eq. (26).

One can think of Eq. (39) as an extension of Whittle's likelihood, accounting for window or averaging distortions (using  $\bar{S}$  instead of  $S$ ) and correlations between frequencies within the segments (using  $\nu$  instead of twice the number of averaged periodograms). Using  $S$  instead of  $\bar{S}$  may lead to bias in parameter estimates, whereas using the number of averaged periodograms instead of  $\nu$  may lead to underestimated parameter uncertainties. Besides, this formulation does not account for correlations between *averaged* periodograms at different central frequencies  $j$ .

For well-chosen windows and  $L$  sufficiently large, the approximation  $\bar{S}_L \approx S$  is acceptable. However, we see from Fig. 1 that changes in the variance may be significant. Any inference of parameters describing the PSD will yield standard deviations that are underestimated by a factor  $\nu/(2M)$ .

#### D. Bias estimation

The optimal bias-variance trade-off depends on the specific focus of the analysis. For example, if the aim is to estimate the parameters of a low-frequency component, the optimal binning will be coarser than if the aim is to estimate a parameter that drives the high-frequency end of the spectrum.

For any given parameter and an associated likelihood model, Fisher's information provides a forecast of parameter errors, or at least a lower bound. Let us assume that the PSD is parametrized by a vector of  $p$  parameters  $\boldsymbol{\theta}$ , so that  $S = S(f, \boldsymbol{\theta})$ . The Fisher information matrix has entries

$$I_{lm}(\boldsymbol{\theta}) = -\mathbb{E} \left[ \frac{\partial \mathcal{L}}{\partial \theta_l \partial \theta_m} \right], \quad (40)$$

where  $\mathcal{L}$  is the log-likelihood. Using the extended Whittle's likelihood in Eq. (39) for  $\mathcal{L} = \log f_{\bar{P}}$ , and assuming  $\bar{S}(f) \approx S(f)$ , one obtains

$$I_{lm}(\boldsymbol{\theta}) = \frac{\nu}{2} \sum_{j=j_{\min}}^{j_{\max}} \frac{1}{S(f_j)^2} \frac{\partial S(f_j)}{\partial \theta_l} \frac{\partial S(f_j)}{\partial \theta_m}. \quad (41)$$

Besides forecasting statistical uncertainties, estimating the bias can be of key interest when choosing the characteristics of spectral estimates, like the level of smoothing. We can proceed similarly to Cutler & Vallisneri [28]. In their work, the authors evaluate the parameter errors when using inaccurate GW waveform templates. For SGWB searches, we rather focus on parametric PSDs. We introduce the best-fit parameter  $\boldsymbol{\theta}_{\text{bf}}$ , i.e., the one that maximizes the log-likelihood  $\mathcal{L}$ . We have, by definition:

$$\nabla \mathcal{L}(\boldsymbol{\theta}_{\text{bf}}) = \mathbf{0}, \quad (42)$$

where  $\nabla \mathcal{L}$  denotes the log-likelihood gradient.

We label the actual parameter describing the analysed data (the one that drives the stochastic process generation) as  $\boldsymbol{\theta}_{\text{tr}}$ . We want to evaluate the difference  $\Delta \boldsymbol{\theta} = \boldsymbol{\theta}_{\text{bf}} - \boldsymbol{\theta}_{\text{tr}}$ , which is the error made when using the theoretical PSD  $S(f)$  instead of  $\bar{S}(f)$  in the likelihood, i.e., when ignoring the effects of averaging and windowing effects on the periodogram expectation. We show in Sec. D that an estimate of this error is

$$\Delta \boldsymbol{\theta} \approx \mathbf{I}(\boldsymbol{\theta}_{\text{bf}})^{-1} \mathbf{B}, \quad (43)$$

where  $\mathbf{B}$  is the  $p$ -column vector whose entries are

$$B_l \equiv \frac{\nu}{2} \sum_{j=j_{\min}}^{j_{\max}} \frac{\partial S(f_j)}{\partial \theta_l} \frac{\text{Bias}[\bar{P}(f_j) | \boldsymbol{\theta}_{\text{tr}}]}{S(f_j, \boldsymbol{\theta}_{\text{bf}})^2}, \quad (44)$$

which unsurprisingly depends on the spectrum bias introduced in Eq. (31). Note that this result generalizes to any type of inaccuracies of the PSD template, including physical modeling errors. In addition, to leading order,  $\boldsymbol{\theta}_{\text{tr}}$  can be replaced by  $\boldsymbol{\theta}_{\text{bf}}$  in Eq. (44). This is convenient when performing an a-posteriori assessment where the true parameter is unknown.

#### E. The multivariate case: covariance and spectral estimate

Up to now, we have considered a single observable in the time series. This section addresses the case of the joint analysis of several time series representing different observables. This is essential in multi-detector ground-based searches for stochastic GWs [2], where the use of multiple measurements enables disentangling signal and noise. This will also be the case of third-generation detectors in triangular configuration, although noise-sourced correlations have to be addressed [35]. LISA faces the same challenge, where any complete set of variables necessary for science extraction exhibits cross-correlations due to both noise and signal. This is the case of the Michelson TDI variables  $X, Y, Z$  [36]. We consider them as three dependent, stationary, and Gaussian-distributed time series of length  $N$ , represented by three column vectors  $\mathbf{x}, \mathbf{y}, \mathbf{z}$ . We can form the full data vector of size  $3N$  as  $\mathbf{d} = (\mathbf{x}^{\top}, \mathbf{y}^{\top}, \mathbf{z}^{\top})^{\top}$ .

The frequency-domain covariance matrix of  $\tilde{\mathbf{d}}$  can be partitionned into  $N \times N$  blocks

$$\tilde{\Sigma}_d = \begin{pmatrix} \tilde{\Sigma}_{xx} & \tilde{\Sigma}_{xy} & \tilde{\Sigma}_{xz} \\ \tilde{\Sigma}_{yx} & \tilde{\Sigma}_{yy} & \tilde{\Sigma}_{yz} \\ \tilde{\Sigma}_{zx} & \tilde{\Sigma}_{zy} & \tilde{\Sigma}_{zz} \end{pmatrix} \quad (45)$$

where

$$\tilde{\Sigma}_{\alpha\beta} \equiv \text{Cov}(\tilde{\alpha}, \tilde{\beta}) \quad \forall \alpha, \beta \in \{x, y, z\}. \quad (46)$$

We can write down an expression for the element of the block matrices by generalizing Eq. (4):

$$\tilde{\Sigma}_{\alpha\beta}(i, j) = \frac{1}{2} \int_{-\frac{f_s}{2}}^{+\frac{f_s}{2}} \tilde{w}(f_i - f) \tilde{w}^*(f_j - f) S_{\alpha\beta}(f) df, \quad (47)$$

where  $S_{\alpha\beta}(f)$  designates the cross spectral density (CSD) function when  $\alpha \neq \beta$ . This multivariate data can also be modelled as a Gaussian distribution of the same form as Eq. (34).

We define the periodogram matrix as the  $3 \times 3$  frequency-dependent matrix

$$\mathbf{P}_N(f_k) \equiv \frac{2}{\tau_s \kappa_N} \tilde{\mathbf{d}}(f_k) \tilde{\mathbf{d}}(f_k)^\dagger, \quad (48)$$

where  $\tilde{\mathbf{d}}(f_k)$  is the  $3 \times 1$  column vector representing the DFT of the TDI channels evaluated at frequency bin  $f_k$ .

Like in the univariate case, we can consider short segments in the time or frequency domain. Without loss of generality, we focus on frequency-domain segments here. Instead of averaging over scalar periodograms, we need to average over sample covariance matrices. This way, we define an averaged  $3 \times 3$  periodogram matrix for each frequency segment:

$$\bar{\mathbf{P}}(f_j) \equiv \frac{1}{N_j} \sum_{k=j-K_j}^{j+K_j} \mathbf{P}_N(f_k). \quad (49)$$

The individual sample covariances entering the sum are usually correlated due to finite windowing, like in the univariate case.

## F. Multivariate approximate likelihood

We saw that in the univariate case, one can approximate the averaged periodogram as a random variable proportional to a chi-squared distributed variable. The generalization of this approximation in the multivariate case amounts to assuming that  $\bar{\mathbf{P}}$  is proportional to a Wishart distribution with an effective number of degrees of freedom  $n = \nu/2$ . The PDF then writes

$$f_{\bar{P}}(\bar{\mathbf{P}}) = \frac{|\bar{\mathbf{P}}|^{n-3} e^{-n \text{tr}(\mathbf{C}^{-1} \bar{\mathbf{P}})}}{|n^{-1} \mathbf{C}|^n \cdot \mathcal{C}\tilde{\Gamma}_p(n)}, \quad (50)$$

where  $\mathcal{C}\tilde{\Gamma}_p(n)$  is the complex multivariate Gamma function. After dropping the constant terms, one can write the log-PDF of  $\bar{\mathbf{P}}$  as

$$\log f_{\bar{P}} = - \sum_{j=j_{\min}}^{j_{\max}} \frac{\nu_j}{2} (\log |\mathbf{C}(f_j)| + \text{tr}(\mathbf{C}(f_j)^{-1} \bar{\mathbf{P}}(f_j))) \quad (51)$$

where the frequency-dependent matrix  $\mathbf{C}(f)$  is Hermitian and has dimension  $3 \times 3$  with elements  $\mathbf{C}_{\alpha\beta}(f) = S_{\alpha\beta}(f)$  for  $\alpha \leq \beta$ . Note that this formulation ignores windowing effects, as we assume that the covariance blocks  $\tilde{\Sigma}_{\alpha\beta}$  are diagonal and their diagonal elements are assimilated to the PSDs and CSDs.

## G. Multivariate bias estimate

The multivariate version of the Fisher matrix in Eq. (41) can be written as

$$I_{lm}(\boldsymbol{\theta}) = \sum_{j=j_{\min}}^{j_{\max}} \frac{\nu_j}{2} \text{tr} \left( \mathbf{C}(f_j)^{-1} \frac{\partial \mathbf{C}(f_j)}{\partial \theta_l} \mathbf{C}(f_j)^{-1} \frac{\partial \mathbf{C}(f_j)}{\partial \theta_m} \right). \quad (52)$$

Equation (43) for the parameter bias remains the same, where the elements of vector  $\mathbf{B}$  are now given by

$$B_l = \sum_{j=j_{\min}}^{j_{\max}} \frac{\nu_j}{2} \text{Tr} \left( \mathbf{C}(f_j, \boldsymbol{\theta}_{\text{bf}})^{-1} \frac{\partial \mathbf{C}(f_j)}{\partial \theta_l} \mathbf{C}(f_j, \boldsymbol{\theta}_{\text{bf}})^{-1} \text{Bias}[\bar{\mathbf{P}}(f_j) | \boldsymbol{\theta}_{\text{tr}}] \right) \quad (53)$$

The spectrum bias is now a  $3 \times 3$  matrix defined as the difference between the periodogram expectation and the spectrum matrix:

$$\text{Bias}[\bar{\mathbf{P}}(f_j) | \boldsymbol{\theta}_{\text{tr}}] = \mathbf{E}[\bar{\mathbf{P}}(f_j) | \boldsymbol{\theta}_{\text{tr}}] - \mathbf{C}(f_j, \boldsymbol{\theta}_{\text{tr}}). \quad (54)$$

We apply this formalism to the case of SGWB searches in Sec. VII.

## VI. ACCOUNTING FOR NON-STATIONARITY

### A. Covariance and spectral estimate

In this section, we extend the discussion to locally-stationary multivariate processes. Following [37], one can describe a general Gaussian non-stationary process by its autocovariance function as

$$\mathbf{R}(t, s) = \boldsymbol{\gamma} \left( \frac{t+s}{2}, t-s \right), \quad (55)$$

where  $\boldsymbol{\gamma}$  is a function of the middle time and the time difference of two time points  $t$  and  $s$ . Note that for a multivariate process,  $\mathbf{R}$  is a square matrix of dimension

$p$ , where  $p$  is the number of channels. We can then define an evolutionary spectrum as the Fourier transform of  $\gamma$ :

$$\mathbf{C}(u, f) = \int_{-\infty}^{+\infty} \gamma(u, v) e^{-2i\pi fv} dv. \quad (56)$$

Consider a time point, denoted by  $\tau$ . For a locally stationary process, the stationary assumption is only valid in the neighborhood of  $\tau$ , i.e., within an interval of size  $l(\tau)$  around  $\tau$ . In this interval, we can make the approximation that the autocovariance function depends only on the difference between two time points. Formally, this statement can be expressed as follows:

$$\forall t \in [\tau - l(\tau)/2, \tau + l(\tau)/2], \\ \mathbf{R}(t, s) \approx \gamma(\tau, t - s) \quad \forall s. \quad (57)$$

The spectral consequence of this approximation is that for any point  $(\tau, \xi)$  in the time-frequency plane, there is a rectangular box  $I(\tau, \xi)$  around that point where the spectrum is approximately constant. Hence,  $\forall(t, f) \in I(\tau, \xi)$ , we have  $\mathbf{C}(t, f) \approx \mathbf{C}(\tau, \xi)$ . This box is a rectangle of size  $l(\tau) \times 1/d(\tau)$ , where  $d(\tau)$  is the decorrelation length (which verifies  $d(\tau) < l(\tau)/2$ ).

Let us now consider the periodogram  $P_L^m(f_k)$  defined in Eq. (11), centered on some time point  $t_m$ , computed over a length  $L$  equal to or smaller than the local stationary scale  $l$ . Similarly to Welch's periodogram expectation, it follows directly from Eq. (47) that

$$\mathbb{E} [\mathbf{P}_{L \leq l}^m(f_k)] = \frac{1}{\tau_s \kappa_L} \int_{-\frac{f_s}{2}}^{+\frac{f_s}{2}} |\tilde{w}_L(f_k - f)|^2 \mathbf{C}(t_m, f) df, \quad (58)$$

which now depends on the time-varying spectrum matrix  $\mathbf{C}(t_m, f)$ .

## B. Time-frequency approximate likelihood

As for the stationary case, we can approximate the distribution of  $\mathbf{P}_L^m(f_k)$  (or an averaged version of it) with a Wishart distribution:

$$\log f_{\bar{\mathbf{P}}} = - \sum_{m,j} \frac{\nu_j}{2} (\log |\mathbf{C}(t_m, f_j)| \\ + \text{tr} (\mathbf{C}(t_m, f_j)^{-1} \mathbf{P}_L^m(f_j))), \quad (59)$$

where we dropped the interval on which the time and frequency indices  $m, j$  run for clarity. This means that the periodogram evaluated at a frequency bin  $f_j$  computed over a time chunk centered on  $t_m$  approximately follows a Wishart distribution with  $\nu_j/2$  degrees of freedom, where the value of  $\nu_j$  depends on the averaging that goes into the computation of the periodogram.

## C. Time-frequency bias estimate

One can estimate the bias of any mismodelling of the spectrum  $\mathbf{C}(t, f)$  of a locally stationary process by using the same formula as in Eq. (43). The only difference is that one must replace  $\mathbf{C}(f_j)$  by  $\mathbf{C}(t_m, f_j)$  in Eqs. (52) and (53).

A possible source of bias in time-frequency analysis is inappropriate time binning. This issue arises when computing periodograms over a length  $L$  that is greater than the stationary timescale  $l$ . In such a situation, the time resolution is too coarse to account for short-scale variations in the spectrum. The resulting periodogram therefore reflects average behavior over the period it is computed. In that case, the periodogram expectation in Eq. (58) can be computed by replacing  $\mathbf{C}(t_m, f)$  by an average over the considered period:

$$\mathbb{E} [\mathbf{P}_{L > l}^m(f_k)] = \frac{1}{\tau_s \kappa_L} \int_{-\frac{f_s}{2}}^{+\frac{f_s}{2}} |\tilde{w}_L(f_k - f)|^2 \mathbf{C}_L(t_m, f) df, \quad (60)$$

where we set

$$\mathbf{C}_L(t_m, f) = \frac{1}{L \tau_s} \int_{t_m - L \tau_s/2}^{t_m + L \tau_s/2} \mathbf{C}(t, f) dt. \quad (61)$$

To estimate the bias due to a coarse gridding in time, one can use the difference between the periodogram expectation and the time-frequency covariance model evaluated at  $t_m$ :

$$\text{Bias}[\mathbf{P}(t_m, f_j) | \boldsymbol{\theta}_{\text{tr}}] = \mathbb{E} [\mathbf{P}_{L > l}^m(f_k)] - \mathbf{C}(t_m, f). \quad (62)$$

In the way similar to frequency-domain averaging, the bias depends on the second time derivatives of the spectrum. One can then directly plug Eq. (62) into Eq. (53) to assess the bias on parameters controlling the covariance model. This is what we do in Sec. VIII.

## VII. APPLICATION TO FREQUENCY BINNING IN SGWB SEARCHES

We apply the bias estimate presented in Sec. V to assess the error due to binning in the frequency domain when searching for a SGWB in LISA data.

### A. Simulated data

We use the same LISA noise configuration as the in the Cosmo dataset NOISE-1A [38] available on the LISA Data Challenges (LDC) website [39]. It includes a year of TDI instrumental noise sampled at 0.5 Hz and generated with the package LISA INSTRUMENT [40]. Spacecraft orbits are assumed to follow Keplerian orbits that minimize flexing to leading order in eccentricity, such that arm lengths are approximately constant and equal.

We add an isotropic gravitational wave stochastic signal representing the radiation from cosmic strings. The parameter values are the same as in the dataset “SGWB cosmic strings 1a”, or cs-1A, also downloadable from the LDC website. Its all-sky all-polarization power spectral density is

$$S_h(f) = \Omega(f) \frac{3H_0^2}{4\pi^2 f^3}, \quad (63)$$

where  $\Omega(f)$  is the background energy density per logarithmic frequency parameterized as

$$\Omega(f) = 0.55 \times 10^{-11} \left( \frac{G\mu}{10^{-13}} \right)^{1/2} \left( \frac{f}{f_p} \right)^n, \quad (64)$$

with  $f_p = 3 \times 10^{-3}$  Hz,  $n = 0$  and  $G\mu = 10^{-13}$ . In the cs-1A dataset, the SGWB is simulated with LISA GW RESPONSE [41]. Note that the simulation available in the LDC website has a missing factor of  $\sqrt{H_0}$  for the SGWB amplitude, which we reapply to be consistent with Eq. (63).

## B. Analysis covariance model

We use a simple parametrized covariance model with three components: a low-frequency noise component, or test mass (TM) noise, a high-frequency noise component, or optical metrology system (OMS) noise, and a GW background described by a power law, whose SNR peaks in the middle of the band. We assume that all component spectral shapes are known, but their respective amplitudes must be estimated. The covariance model for the Michelson TDI variables can be written as

$$\mathbf{C}_d(f) = \sum_l \alpha_l \mathbf{C}_l(f), \quad (65)$$

where  $\alpha_l$  are the PSD coefficients to be estimated, and the index runs on all components of the model  $l = \{\text{OMS}, \text{TM}, \text{GW}\}$ . We build the noise covariance matrices  $\mathbf{C}_l$  based on the model presented in [42], and the GW covariances are built as in [10].

As an illustration, we plot in Fig. 5 the three contributions of the first diagonal element of the covariance model (the PSD of  $X$ ). The figure shows the OMS contribution, which mostly contributes to high frequencies, the TM contribution that dominates low frequencies, and the SGWB signal, which in this case reaches its highest SNR at mid-frequencies around 3 mHz.

## C. Forecast of the bias due to periodogram averaging

After taking the DFT of the year-long time series, we select the bandwidth between 0.1 and 28 mHz, whose limits correspond respectively to the lower bound of the

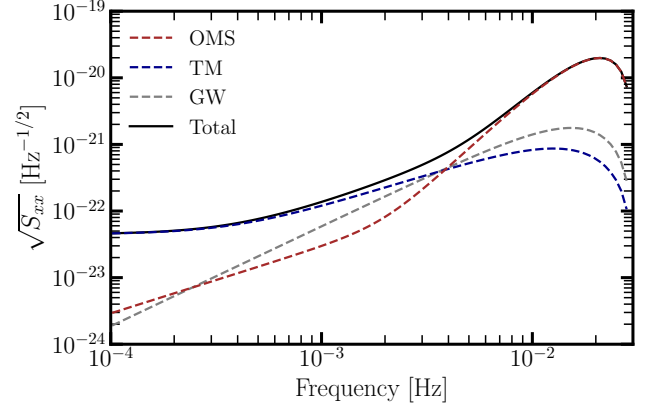


FIG. 5. Components of the TDI  $X$  PSD: OMS noise (dashed red), TM noise (dashed blue), SGWB (dashed gray), and sum (solid black).

LISA sensitive band and the first dip of the response with a safe margin. We then split the bandwidth into  $J$  segments of constant size  $N_j = N_{\text{seg}}$  and form the binned periodogram  $\tilde{P}_N(f)$  following the averaging process outlined in Sec. IV. We define the averaging bandwidth as  $N_{\text{seg}}/T$ , where  $T$  is the observation time. Our goal is to choose an averaging bandwidth as large as possible for computational efficiency while keeping the induced bias below the statistical error.

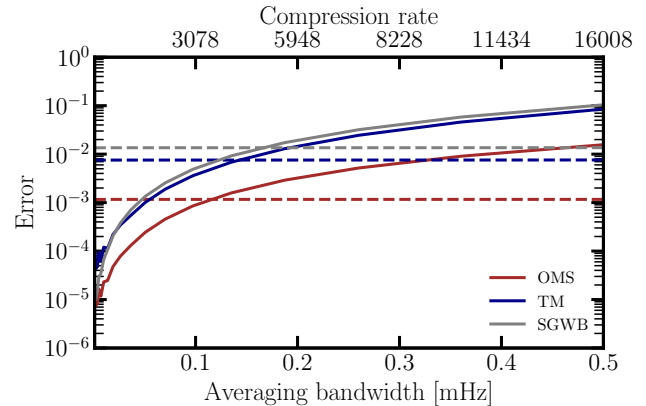


FIG. 6. Bias and standard deviation of amplitude parameters as a function of the averaging bandwidth (lower axis) and compression rate (upper axis).

We test 20 averaging bandwidths logarithmically sampled from  $10^{-6}$  Hz to  $5 \times 10^{-2}$  Hz for which we evaluate the parameter standard deviations using Eq. (52) and their bias using Eq. (43). They correspond to compression rates ranging from 31 to 16008 relative to the native frequency grid sampled every  $1/T$ . We report the results in Fig. 6.

Dashed lines represent standard deviations for OMS (red), TM (blue), and GW (gray) amplitudes  $\alpha_l$ . As

we analyze the same frequency bandwidth, they remain constant when we change the averaging bandwidth. Solid lines represent the amplitude bias, using the same color code. It increases with the averaging bandwidth. For each parameter, the closer the bias is to the standard deviation, the more significant it becomes compared to statistical errors. Based on this plot, one can state that using frequency segments smaller than 0.1 mHz in width will result in negligible bias for all parameters. However, averaging over a width of 0.2 mHz would induce a significant bias, at least for noise parameters. For an even more aggressive averaging, like 0.4 mHz, the bias should be larger than the statistical errors for all parameters.

In Fig. 6 we see that the bias increases monotonically with the averaging bandwidth. This is not necessarily a general behaviour, as it could undergo local drops depending on the spectral shapes of the model components and how their second derivative varies with frequency.

#### D. Bias verification with posterior sampling

We test the bias forecast of Fig. 6 by running a Bayesian inference of the three parameters  $\alpha_l$  with uniform priors in the range  $[-2, 2]$ . We use the Wishart likelihood in Eq. (51). We perform two inferences: in the first one, we use “noiseless” data: the data periodogram matrix  $\bar{\mathbf{P}}(f)$  in the likelihood is taken equal to its statistical expectation  $E[\bar{\mathbf{P}}(f)]$ . This provides a reference that is independent of statistical fluctuations. In the second inference, we directly use the periodogram matrix computed from noise and signal realizations obtained by combining the NOISE-1A and CS-1A data. The injection corresponds to parameter values  $\alpha_l = 1$  for all components  $l$ . We perform the inference for three choices of averaging bandwidth: 0.05 mHz, 0.2 mHz, and 0.4 mHz. These are referred to as high, medium, and low resolution, respectively.

We use the ERYN ensemble sampler [43–45] with 12 walkers to explore the posterior distribution. After a burn-in phase of 2000 steps, we collect 500 posterior samples by recording every other 5 steps. We plot the marginalized posteriors in Fig. 7 for the three cases of averaging bandwidth. Each column corresponds to one parameter, while each row (and color) corresponds to an averaging bandwidth. The vertical dashed lines indicate the values  $\alpha_l + \Delta\alpha$  where  $\Delta\alpha$  is the bias predicted by Eq. (43). The smooth, solid line distributions represent “noiseless” posteriors, whereas step histograms represent posteriors obtained with one data realization (LDC data). All lines are aligned with the smooth posterior modes, confirming the reliability of the bias forecast at first order. The posteriors obtained with the data realization are consistent with the “noiseless” ones within statistical errors. This means that the analytical modeling of the covariance agrees with the simulated data, even though the two were generated independently using time-domain simulators.

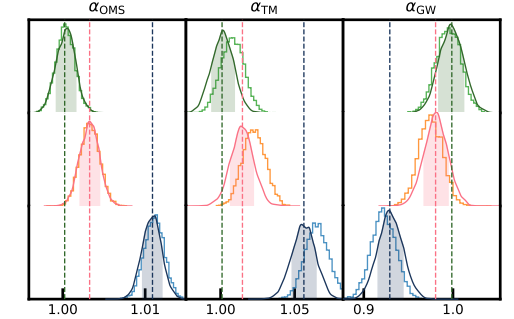


FIG. 7. From top to bottom, the rows correspond to marginalized parameter posteriors for averaging bandwidths of 0.05 (green), 0.2 (red), and 0.4 mHz (blue). From left to right, the three columns correspond to coefficients for the OMS, TM, and GW components in the covariance. Vertical dashed lines are biased values predicted by Eq. (43), to be compared with the injected value which is  $\alpha_l = 1$  for all parameters. The smoothed PDF represent the zero-noise posteriors, while the histograms show the distributions obtained from LDC data simulations. This plot was realized with CHAINCONSUMER [46].

The high-resolution case (green) exhibits a negligible bias since both vertical lines and posteriors are almost aligned with the injected values  $\alpha_l = 1$ . Departures from one become visible for all parameters when using the medium resolution (red), but a bias would be hardly distinguishable from statistical errors, especially for the GW component. Using the low resolution (dark blue) induces statistically significant biases, in accordance with the forecast.

## VIII. APPLICATION TO TIME BINNING IN SGWB SEARCHES

### A. Data simulation

In this section, we consider the same instrumental setup as in Sec. VII A except that we use numerically optimized spacecraft orbits featuring larger time variations. The simulation of the spacecraft positions can be retrieved from a repository made available by ESA [47]. The corresponding orbit file is produced by the software LISA ORBITS [48].

We can compute the instrumental noise and SGWB covariance matrices from the orbits. Even though the stochastic sources (SGWB, OMS, and TM noises) are stationary, the dependence of the TDI transfer functions on the light travel times between spacecraft induces a slow non-stationarity in the measured process. We illustrate this by plotting the relative variation of TDI  $X$  PSD divided by its value at the initial time in Fig. 8 at 3 mHz. We observe slow variations of about 5% over one year. Note that the relative variation is different depending on the considered frequency.

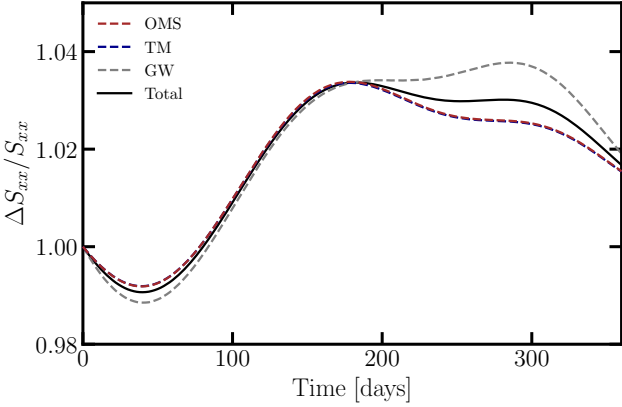


FIG. 8. Variation of TDI X PSD relative to its initial value as a function of time, evaluated at frequency  $f = 3$  mHz. We break it into three components: OMS noise (dashed red), TM noise (dashed blue), SGWB (dashed gray). The relative variation of the total PSD is shown by the solid black line.

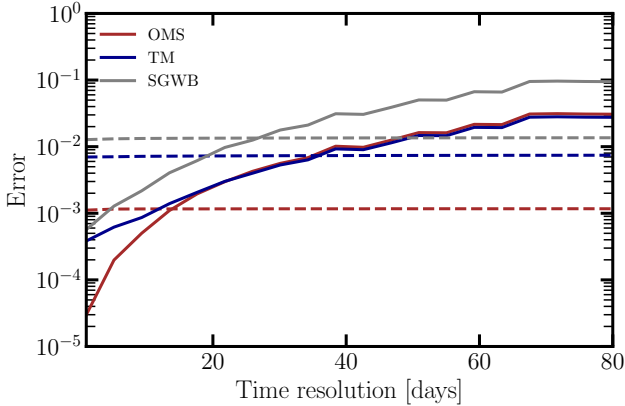


FIG. 9. Bias on spectrum component amplitudes as a function of the resolution of the time chunking for OMS noise (red), TM noise (blue), and SGWB (gray). The solid lines show the parameter biases, while the dashed lines show their standard deviations.

## B. Forecast of the bias due to coarse time gridding

We investigate the effect of time resolution on the accuracy of  $\alpha_l$  parameter inference. We build several time grids  $t_m$  starting from day-long to 80-day-long time chunks. For each of these chunks, we compute the covariance model  $\mathbf{C}(t_m, f)$  and the periodogram expectation  $E[\mathbf{P}_L^m(f)]$  using Eq. (60). We compute the parameter bias using Eq. (43) and report the results in Fig. 9.

The bias remains below or comparable to the statistical error (a few  $\sigma$ ) for chunks that are smaller than 20 days. Above this threshold, the bias starts to be significant relative to the standard deviation, especially for the OMS noise amplitude. For resolutions of 80 days, the bias on the SGWB amplitude reaches nearly 10 times

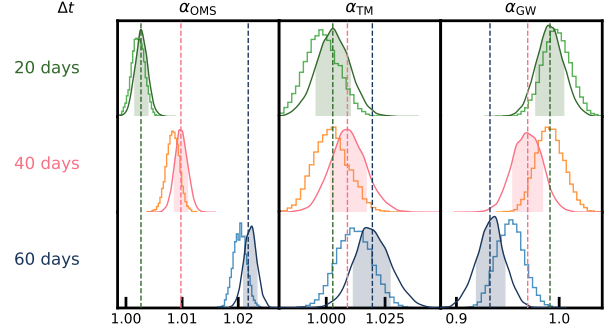


FIG. 10. From top to bottom, the rows correspond to marginalized parameter posteriors for time resolutions of 20 (green), 40 (red), and 60 days (blue). From left to right, the three columns correspond to coefficients for the OMS, TM, and GW components in the covariance. Vertical dashed lines are biased values predicted by Eq. (43), to be compared with the injected value which is  $\alpha_l = 1$  for all parameters. The smoothed PDF represent the zero-noise posteriors, while the histograms show the distributions obtained from the LDC data simulations.

the standard deviation in absolute value. This indicates that accurate inference with LISA data must account for the time variations of the spectrum of noise and signal components, even if the underlying process is originally stationary (and even if the signal source is isotropically distributed over the sky).

We verify this behavior by sampling the posterior using the same uninformative uniform distributions as in Sec. VII D for a selection of 3 time resolutions: 20 days (high resolution), 40 days (medium), and 60 days (low). We plot the marginalized posteriors of amplitude parameters in Fig. 10. Again, the smooth PDFs represent “noiseless” inferences, while the bar histograms are the results obtained with the LDC data realization.

We observe an agreement between the parameter posterior means and the value that the bias estimation predicts, demonstrating the reliability of the approximation for this model. Additionally, the posterior distribution we obtain from the LDC data realization (bar histograms) is also statistically consistent with the posterior obtained from the noiseless likelihood. In the case of high (green) and medium (red) resolutions, the bias is hardly distinguishable from the statistical error, except for the OMS noise amplitude (left panel). The low-resolution analysis (blue) exhibits a clear bias for all parameters, in agreement with the analytical forecast. This is confirmed by the analysis performed on the independently-generated LDC datasets (bar histograms in Fig. 10), where the posterior distributions are in statistical agreement with the “noiseless” posteriors.

Therefore, an analysis that would assume stationarity, or even a time-frequency analysis with an inappropriate time binning, would induce a statistically significant error on isotropic SGWB parameter inference only because of the time variations of the instrument response.

## IX. DISCUSSION

When characterizing the spectrum of stationary or locally stationary time series, it is often useful to define sufficient statistics, i.e., transform the data into a collection of reduced quantities (spectral estimates) that contain the necessary information while being more compact than the original data. We reviewed how correlations between adjacent bins in time or frequency may affect the distribution of spectral estimates. When averaging several periodograms, the statistics of the resulting estimate depend on correlations among periodogram ordinates. The effect of correlations can be approximately accounted for by assuming that the spectrum is a random variable proportional to a chi-squared distribution in the univariate case, or a Wishart distribution in the multivariate case. The number of degrees of freedom of this distribution is set by the number of averaged segments (either in time or frequency) and by the level of correlations between bins. The correlation relates to the shape of the time window and its potential overlap between segments.

We argued that frequency-domain smoothing typically provides greater data compression than time-segment averaging. It also has the advantage of being less susceptible to leakage because the time window size is larger. However, frequency smoothing introduces a bias related to spectral variations across the averaged frequency bandwidth. To mitigate this effect, we showed how to predict the bias in order to achieve the optimal balance between data compression and accuracy. For spectra depending on unknown parameters, we derived a simple estimate of the parameter bias due to frequency binning based on a Taylor expansion up to first order in spectrum derivatives. We gave an example of an application with a simulation of LISA data featuring a mixture of instrumental noises and a SGWB. We were able to determine for which binning the bias can be neglected compared to the statistical error.

Furthermore, we demonstrated that the same bias estimation framework can be applied to handle spectral non-stationarities. In time-frequency data analyses based on the short-term Fourier transform, a time resolution must be chosen that is fine enough to describe the characteristic timescale of the underlying stochastic process. This scale determines the period over which the process can be considered approximately stationary. Coarser time resolutions typically reduce computational complexity and increase the sensitivity to lower frequencies. However, if the resolution is low compared to the stationary length, this directly results in a bias when estimating the spectrum. We demonstrated that, in the case of future LISA data, time-frequency analysis with a resolution finer than 20 days is necessary to avoid any detectable bias induced by modulations of noise and signal TDI transfer functions over one year of data. Note that this result relates only to arm flexing: possible intrinsic noise non-stationarities or sky anisotropies of stochastic GW components are likely

to impose more stringent constraints.

Our analysis demonstrates that performing accurate SGWB searches with detector data requires fine control over correlation effects in time and frequency. We propose a Fisher-information-based tool that provides a method for selecting adapted resolutions based on the expected statistical precision. Beyond binning effects, our analysis can be used to quantify parameter biases arising from any discrepancy between the data and the model.

In this work, we considered the effect of correlations on the statistics of averaged spectral estimates. Although we expect it to be marginal, we ignored the correlations among neighboring averaged periodograms in time or frequency, which allowed us to write down a likelihood that is the product of single-frequency or time-frequency bin likelihoods. In the future, we plan to study the significance of these correlations in the context of SGWB searches, and explore the advantage of using different time-frequency representations like wavelets.

## ACKNOWLEDGMENTS

We acknowledge very insightful discussions with R. Buscicchio, O. Burke and A. Vajpeyi. We also thank F. Pozzoli, M. Muratore, N. Dam Quang, O. Hartwig, M Pieroni, A. Santini, R. Meyer, S. Babak, C. Caprini, H. Inchauspé, A. Petiteau, M. Besançon, and G. Nardini and all the members of the LISA SGWB code comparison team. We are grateful to C. Cavet who maintains the LDC website up and running. NK was supported by the Hellenic Foundation for Research and Innovation (H.F.R.I.) under the 4th Call for HFRI Research Projects to support Post-doctoral Researchers (Project Number: 28418). This work was performed using HPC resources from CNES Computing Center.

## SOFTWARE AND DATA

We have used the `backgrounds` [49] software to perform the inferences and model signal and instrumental responses. We used the `Eryn` [50] sampler to probe the posterior distributions using Markov chain Monte-Carlo. The datasets used in this work can be found on the LDC website at <https://lisa-ldc.in2p3.fr/>.

## Appendix A: Baseline instrumental noise PSD

The instrumental noise PSD used in this work assumes two independent noise sources coming from test-mass (TM) free-fall perturbations affecting low frequencies and optical metrology system (OMS) noise affecting high frequencies. Their spectral shape follow the technical note LISA-LCST-SGS-TN-001[51] derived from the LISA Science Requirement (SciRD), but their amplitude differ

from the SciRD, to match the simulations in the LDC Cosmo dataset. For the test-mass noise we have

$$S_{\text{TM}}(f) = a_{\text{TM}}^2 \left[ 1 + \left( \frac{f_1}{f} \right)^2 \right] \left[ 1 + \left( \frac{f}{f_2} \right)^4 \right], \quad (\text{A1})$$

where  $a_{\text{TM}} = 2.4 \times 10^{-15} \text{ ms}^{-2}$ ,  $f_1 = 4 \times 10^{-4} \text{ Hz}$  and  $f_2 = 8 \text{ mHz}$ . For the OMS readout noise, we have

$$S_{\text{OMS}}(f) = a_{\text{OMS}}^2 \left[ 1 + \left( \frac{f_3}{f} \right)^4 \right], \quad (\text{A2})$$

where  $a_{\text{OMS}} = 7.9 \times 10^{-12} \text{ mHz}^{-1/2}$  and  $f_3 = 2 \text{ mHz}$ .

## Appendix B: Correlations of periodograms of different time segments

In this section, we compute the correlation coefficient between periodograms computed on two different segments  $m$  and  $m'$ , but at a single frequency  $f_k$ , as defined in Eq. (15). We reproduce its definition here:

$$c_{mm'}(f_k) \equiv \frac{\text{Cov} [P_L^m(f_k), P_L^{m'}(f_k)]}{\text{Var} [P_L(f_k)]}. \quad (\text{B1})$$

We start with the denominator. For large enough  $L$ , the variance of a segment periodogram is approximately equal to its squared expectation (see, e.g., [52] or [53]):

$$\text{Var} [P_L(f_k)] \approx \mathbb{E} [P_L(f_k)]^2 \approx S_{xx}(f_k)^2. \quad (\text{B2})$$

Now we consider the numerator of Eq. (15). By using the definition of the Welch's periodogram in Eq. (11), and using Isserlis' theorem [54], one can show that for a zero-mean Gaussian process, the covariance of two spectral estimates evaluated at the same frequencies but computed from two different segments  $m$  and  $m'$  is

$$\begin{aligned} \text{Cov} [P_L^m(f_k), P_L^{m'}(f_k)] &= \left( \frac{2}{\tau_s \kappa_N} \right)^2 \left( \left| \mathbb{E} [\tilde{x}_k^m \tilde{x}_k^{m'*}] \right|^2 \right. \\ &\quad \left. + \left| \mathbb{E} [\tilde{x}_k^m \tilde{x}_k^{m'}] \right|^2 \right). \end{aligned} \quad (\text{B3})$$

This result is recalled in [30], p. 442. The expectation in the first term in Eq. (B3) is the covariance of two segment DFT and can be written as :

$$\begin{aligned} \mathbb{E} [\tilde{x}_k^m \tilde{x}_k^{m'*}] &= \frac{1}{2} \int_{-\frac{f_s}{2}}^{+\frac{f_s}{2}} |\tilde{w}_L(f_k - f)|^2 \\ &\quad \times S_{xx}(f) e^{2i\pi f s(m' - m) \tau_s} df. \end{aligned} \quad (\text{B4})$$

Similarly, the expectation in second term in Eq. (B3) writes

$$\begin{aligned} \mathbb{E} [\tilde{x}_k^m \tilde{x}_k^{m'}] &= \frac{1}{2} \int_{-\frac{f_s}{2}}^{+\frac{f_s}{2}} \tilde{w}_L(f_k - f) \tilde{w}_L(f_k + f) \\ &\quad \times S_{xx}(f) e^{2i\pi f s(m' - m) \tau_s} df. \end{aligned} \quad (\text{B5})$$

Note the difference with Eq. (4): now the expression includes the time shift between the two segments. Now we make two approximations. First, far from the Nyquist and zero frequencies, the second term (Eq. (B4)) can be neglected compared to the first term (Eq. (B4)) [55], due to the fact that the window DFT is strongly picked around zero. Second, if we assume that the PSD is approximately constant in the bandwidth within the maximum of the window  $\tilde{w}_N(f)$ , then we can get it out of the integrals. This gives

$$\mathbb{E} [\tilde{x}_k^m \tilde{x}_k^{m'*}] \approx \frac{1}{2} S_{xx}(f_k) \int_{-\frac{f_s}{2}}^{+\frac{f_s}{2}} |\tilde{w}_L(f_k - f)|^2. \quad (\text{B6})$$

Replacing the window DFT  $\tilde{w}_L$  by its definition leads to

$$\text{Cov} [P_L^m(f_k), P_L^{m'}(f_k)] \approx \frac{S_{xx}(f_k)^2}{\kappa_L^2} \left| \sum_{n=0}^{L-1} w_n w_{n+s|m' - m|} \right|^2 \quad (\text{B7})$$

where in the equation above we assume that  $w_n = 0$  for  $n \geq M$ . Using Eq. (B7) and Eq. (B2), Eq. (15) becomes

$$c_{mm'}(f_k) \approx \frac{1}{\kappa_L^2} \left| \sum_{n=0}^{L-1} w_n w_{n+s|m' - m|} \right|^2 \quad (\text{B8})$$

Now we can compute the sum in Eq. (B10):

$$\begin{aligned} \sum_{m < m'}^{M-1} c_{mm'}(f_k) &= \frac{1}{\kappa_L^2} \sum_{m < m'}^{M-1} \left| \sum_{n=0}^{L-1} w_n w_{n+s|m' - m|} \right|^2 \\ &= \sum_{p=0}^{M-1} (M-p) \frac{1}{\kappa_L^2} \left| \sum_{n=0}^{L-1} w_n w_{n+ps} \right|^2 \\ &= \sum_{p=0}^{M-1} (M-p) \rho(p, s), \end{aligned}$$

where we converted the double sum on  $m$  and  $m'$  in a single sum by setting  $p = m' - m$ , and we defined the normalized window correlation function as in Ref. [31]:

$$\rho(p, s) \equiv \begin{cases} \frac{1}{\kappa_L^2} \left| \sum_{n=0}^{L-1-ps} w_n w_{n+ps} \right|^2 & 1 \leq p \leq \lfloor \frac{M}{s} \rfloor \\ 0 & \text{otherwise.} \end{cases} \quad (\text{B9})$$

Plugging this result into Eq. (19) leads to

$$\nu \approx \frac{2M}{1 + \frac{2}{M} \sum_{p=1}^{M-1} (1 - \frac{p}{M}) \rho(p, s)}. \quad (\text{B10})$$

## Appendix C: Correlations of periodograms at different frequencies

In this section, we derive the expression of the correlation coefficient between the periodograms evaluated at

two different frequencies, defined as

$$\sigma_{kk'} \equiv \frac{\text{Cov}[P_N(f_k), P_N(f_{k'})]}{\sqrt{\text{Var}[P_N(f_k)] \text{Var}[P_N(f_{k'})]}}.$$

The numerator quickly drops to zero after a few bins (as in Fig. 2), so we can restrict the computation to close bins:  $|k - k'| \sim O(10)$ . If the PSD is sufficiently smooth, we have  $\text{Var}[P_N(f_k)] \approx \text{Var}[P_N(f_{k'})] \approx S_{xx}(f_k)^2$ . Considering the numerator, we follow the same rationale as in Sec. B:

$$\begin{aligned} \text{Cov}[P_N(f_k), P_N(f_{k'})] &= \left(\frac{2}{\tau_s \kappa_N}\right)^2 \left( |\mathbb{E}[\tilde{x}_k \tilde{x}_{k'}^*]|^2 \right. \\ &\quad \left. + |\mathbb{E}[\tilde{x}_k \tilde{x}_{k'}]|^2 \right). \end{aligned} \quad (\text{C1})$$

The first expectation term in the parenthesis is directly given by the DFT covariance in Eq. (4). The second term is similar to Eq. (B5), without the complex exponential. The window DFT being sharply peaked around zero, we can make the same approximation as in Sec. B, and we get

$$\mathbb{E}[\tilde{x}_k \tilde{x}_{k'}^*] \approx \frac{1}{2} S_{xx}(f_k) \int_{-\frac{f_s}{2}}^{+\frac{f_s}{2}} \tilde{w}_N(f_k - f) \tilde{w}_N^*(f_{k'} - f) df. \quad (\text{C2})$$

We use the expression for the DFT of the window to get

$$\text{Cov}[P_N(f_k), P_N(f_{k'})] \approx \frac{S_{xx}(f_k)^2}{\kappa_N^2} \left| \sum_{n=0}^{N-1} w_n^2 e^{-\frac{2i\pi(k-k')}{N}} \right|^2. \quad (\text{C3})$$

With this approximation, the correlation coefficient only depends on the window:

$$\sigma_{kk'} \approx \frac{1}{\kappa_N^2} \left| \sum_{n=0}^{N-1} w_n^2 e^{-\frac{2i\pi(k-k')}{N}} \right|^2. \quad (\text{C4})$$

Using this result in Eq. (26) and following the same rationale as in Sec. B leads to a simpler computation of the effective number of DOFs:

$$\nu(f_j) = \frac{2N_j}{1 + \frac{2}{N_j} \sum_{k=1}^{N_j-1} \left(1 - \frac{k}{N_j}\right) r(k)}, \quad (\text{C5})$$

where we defined

$$r(k) \equiv \frac{1}{\kappa_N^2} \left| \sum_{n=0}^{N-1} w_n^2 e^{-\frac{2i\pi k}{N}} \right|^2. \quad (\text{C6})$$

## Appendix D: Estimation of the bias when using inaccurate PSD templates

We derive the bias on the parameter vector  $\boldsymbol{\theta}$  when using a PSD model  $S(f, \boldsymbol{\theta})$  that inaccurately describes the actual statistical expectation of the periodogram.

We start from the likelihood in Eq. (39). The best fit parameter  $\boldsymbol{\theta}_{\text{bf}}$  verifies Eq. (42), which yields

$$\sum_{j=j_{\min}}^{j_{\max}} \frac{1}{S(f_j, \boldsymbol{\theta}_{\text{bf}})^2} \frac{\partial S(f_j)}{\partial \theta_l} (\bar{P}_L(f_j) - S(f_j, \boldsymbol{\theta}_{\text{bf}})) = 0. \quad (\text{D1})$$

At first order in the error, we have

$$S(f, \boldsymbol{\theta}_{\text{tr}}) - S(f, \boldsymbol{\theta}_{\text{bf}}) = -\nabla S(\boldsymbol{\theta}_{\text{bf}})^T \Delta \boldsymbol{\theta}, \quad (\text{D2})$$

where  $\nabla S$  is the gradient of the PSD with respect to  $\boldsymbol{\theta}$ . Plugging Eq. (D2) into Eq. (D1) yields

$$\frac{\nu}{2} \sum_{j=j_{\min}}^{j_{\max}} \frac{1}{S(f_j, \boldsymbol{\theta}_{\text{bf}})^2} \frac{\partial S(f_j)}{\partial \theta_l} \quad (\text{D3})$$

$$(\bar{P}_L(f_j) - S(f_j, \boldsymbol{\theta}_{\text{tr}}) - \nabla S(\boldsymbol{\theta}_{\text{bf}})^T \Delta \boldsymbol{\theta}) = 0. \quad (\text{D4})$$

We are interested in the average error, which is the bias without the effect the statistical uncertainty. To that end, we take the expectation of Eq. (D3), which amounts to replacing  $\bar{P}_L(f_j)$  by its expectation  $\mathbb{E}[\bar{P}_L(f_j) | \boldsymbol{\theta}_{\text{tr}}]$  in the equation. We get

$$\begin{aligned} &\frac{\nu}{2} \sum_{j=j_{\min}}^{j_{\max}} \frac{1}{S(f_j, \boldsymbol{\theta}_{\text{bf}})^2} \frac{\partial S(f_j)}{\partial \theta_l} (\mathbb{E}[\bar{P}_L(f_j) | \boldsymbol{\theta}_{\text{tr}}] - S(f_j, \boldsymbol{\theta}_{\text{tr}})) \\ &= \frac{\nu}{2} \sum_{j=j_{\min}}^{j_{\max}} \frac{1}{S(f_j, \boldsymbol{\theta}_{\text{bf}})^2} \frac{\partial S(f_j)}{\partial \theta_l} \nabla S(\boldsymbol{\theta}_{\text{bf}})^T \Delta \boldsymbol{\theta} \\ &= \sum_{m=1}^p \frac{\nu}{2} \sum_{j=j_{\min}}^{j_{\max}} \frac{1}{S(f_j, \boldsymbol{\theta}_{\text{bf}})^2} \frac{\partial S(f_j)}{\partial \theta_l} \frac{\partial S(\boldsymbol{\theta}_{\text{bf}})}{\partial \theta_m} \Delta \theta_m \\ &= \mathbf{I}(\boldsymbol{\theta}_{\text{bf}}) \Delta \boldsymbol{\theta} \end{aligned} \quad (\text{D5})$$

Inverting this relation yields

$$\Delta \boldsymbol{\theta} = \mathbf{I}(\boldsymbol{\theta}_{\text{bf}})^{-1} \mathbf{B}, \quad (\text{D6})$$

where  $\mathbf{B}$  is the  $p$ -column vector defined by

$$B_l \equiv \frac{\nu}{2} \sum_{j=j_{\min}}^{j_{\max}} \frac{1}{S(f_j, \boldsymbol{\theta}_{\text{bf}})^2} \frac{\partial S(f_j)}{\partial \theta_l} \text{Bias}[\bar{P}_L(f_j) | \boldsymbol{\theta}_{\text{tr}}]. \quad (\text{D7})$$

In the expression above, we use the spectrum bias as in Eq. (31), i.e., the difference between the periodogram expectation and the target PSD:

$$\text{Bias}[\bar{P}_L(f_j) | \boldsymbol{\theta}_{\text{tr}}] = \mathbb{E}[\bar{P}_L(f_j) | \boldsymbol{\theta}_{\text{tr}}] - S(f_j, \boldsymbol{\theta}_{\text{tr}}). \quad (\text{D8})$$

- 
- [1] N. Christensen, *Reports on Progress in Physics* **82**, 016903 (2019), publisher: Institute of Physics Publishing.
- [2] J. D. Romano and Neil. J. Cornish, *Living Reviews in Relativity* **20**, 2 (2017).
- [3] LIGO Scientific Collaboration and Virgo Collaboration, J. Aasi, J. Abadie, *et al.*, *Physical Review D* **91**, 022003 (2015).
- [4] B. Abbott, R. Abbott, T. Abbott, *et al.*, *Physical Review D* **100**, 061101 (2019).
- [5] A. Nuttall and G. Carter, *Proceedings of the IEEE* **70**, 1115 (1982).
- [6] P. Welch, *IEEE Transactions on Audio and Electroacoustics* **15**, 70 (1967).
- [7] B. P. Abbott, R. Abbott, T. D. Abbott, *et al.*, *Physical Review Letters* **118**, 121101 (2017), publisher: American Physical Society.
- [8] C. Caprini, D. G. Figueira, R. Flauger, *et al.*, *Journal of Cosmology and Astroparticle Physics* **2019** (11), 017, publisher: IOP Publishing.
- [9] R. Flauger, N. Karesis, G. Nardini, *et al.*, *Journal of Cosmology and Astroparticle Physics* **2021** (1), publisher: IOP Publishing Ltd.
- [10] Q. Baghi, N. Karesis, J.-B. Bayle, *et al.*, *Journal of Cosmology and Astroparticle Physics* **2023** (04), 066, publisher: IOP Publishing.
- [11] A. Santini, M. Muratore, J. Gair, and O. Hartwig, A flexible, GPU-accelerated approach for the joint characterization of LISA instrumental noise and Stochastic Gravitational Wave Backgrounds (2025), arXiv:2507.06300 [gr-qc].
- [12] R. Buscicchio, F. Pozzoli, D. Chirico, and A. Sesana, The first year of LISA Galactic foreground (2025), arXiv:2511.03604 [astro-ph].
- [13] N. Karesis, M. Lilley, and A. Petiteau, *Classical and Quantum Gravity* **37**, 215017 (2020), publisher: IOP Publishing.
- [14] M. Hindmarsh, D. C. Hooper, T. Minkinen, and D. J. Weir, Recovering a phase transition signal in simulated LISA data with a modulated galactic foreground (2024), arXiv:2406.04894 [astro-ph, physics:gr-qc].
- [15] L. Sala and S. Vitale, Precision spectral estimation at sub-hz frequencies: closed-form posteriors and bayesian noise projection (2025), arXiv:2507.20846 [astro-ph.IM].
- [16] C. Talbot, E. Thrane, S. Biscoveanu, and R. Smith, *Physical Review Research* **3**, 043049 (2021).
- [17] LISA adoption announcement, [https://www.esa.int/Science\\_Exploration/Space\\_Science/Capturing\\_the\\_ripples\\_of\\_spacetime\\_LISA\\_gets\\_go-ahead/](https://www.esa.int/Science_Exploration/Space_Science/Capturing_the_ripples_of_spacetime_LISA_gets_go-ahead/) (2024), accessed: 2026-01-19.
- [18] M. R. Adams and N. J. Cornish, *Physical Review D* **89**, 022001 (2014), publisher: American Physical Society.
- [19] G. Boileau, A. Lamberts, N. Christensen, *et al.*, *Monthly Notices of the Royal Astronomical Society* **508**, 803 (2021).
- [20] G. Boileau, A. Lamberts, N. Christensen, *et al.*, *Monthly Notices of the Royal Astronomical Society* **508**, 803 (2021).
- [21] A. W. Criswell, S. Rieck, and V. Mandic, *Templated Anisotropic Analyses of the LISA Galactic Foreground* (2024), arXiv:2410.23260.
- [22] A. W. Criswell, S. Banagiri, J. Lawrence, *et al.*, Flexible Spectral Separation of Multiple Isotropic and Anisotropic Stochastic Gravitational Wave Backgrounds in LISA (2025), arXiv:2508.20308 [astro-ph].
- [23] R. Buscicchio, A. Klein, V. Korol, *et al.*, *The European Physical Journal C* **85**, 887 (2025).
- [24] F. Pozzoli, R. Buscicchio, A. Klein, *et al.*, *Physical Review D* **111**, 063005 (2025).
- [25] O. Burke, S. Marsat, J. R. Gair, and M. L. Katz, *Phys. Rev. D* **111**, 124053 (2025).
- [26] N. J. Cornish, Non-stationary noise in gravitational wave analyses: The wavelet domain noise covariance matrix (2025), arXiv:2511.10632 [gr-qc].
- [27] S. J. Vigeland and M. Vallisneri, *Monthly Notices of the Royal Astronomical Society* **440**, 1446 (2014).
- [28] C. Cutler and M. Vallisneri, *Phys. Rev. D* **76**, 104018 (2007).
- [29] L. C. Astfalck, A. M. Sykulski, and E. J. Cripps, *Biometrika* **111**, 1313 (2024), eprint: <https://academic.oup.com/biomet/article-pdf/111/4/1313/60783792/asae033.pdf>.
- [30] D. B. Percival and A. T. Walden, *Spectral Analysis for Univariate Time Series*, Cambridge Series in Statistical and Probabilistic Mathematics (Cambridge University Press, Cambridge, 2020).
- [31] *PSD computations using Welch's method*, Tech. Rep. SAND-91-1533 (Sandia National Lab. (SNL-NM), Albuquerque, NM (United States), 1991).
- [32] F. Nobile, M. Bellotti, R. Buscicchio, *et al.* (2026), manuscript in preparation.
- [33] D. Quang Nam, J. Martino, Y. Lelièvre, *et al.*, *Physical Review D* **108**, 082004 (2023).
- [34] A. M. Sykulski, S. C. Olhede, A. P. Guillaumin, *et al.*, *Biometrika* **106**, 251 (2019).
- [35] I. Caporali, G. Capurri, W. Del Pozzo, *et al.*, *Physical Review D* **112**, 022005 (2025).
- [36] M. Tinto and S. V. Dhurandhar, *Living Reviews in Relativity* **24**, 1 (2020).
- [37] S. Mallat, G. Papanicolaou, and Z. Zhang, *The Annals of Statistics* **26**, 1 (1998), publisher: Institute of Mathematical Statistics.
- [38] J.-B. Bayle, 10.5281/zenodo.15698080 (2025).
- [39] <https://lisa-1dc.in2p3.fr/>.
- [40] J.-B. Bayle, O. Hartwig, and M. Staab, *LISA Instrument* (2023).
- [41] J.-B. Bayle, Q. Baghi, A. Renzini, and M. Le Jeune, *Lisa gw response* (2025).
- [42] N. Karesis, Q. Baghi, J.-B. Bayle, and N. Galanis, Effect of noise characterization on the detection of mhz stochastic gravitational waves (2026), arXiv:2601.19741 [gr-qc].
- [43] N. Karesis, M. L. Katz, N. Korsakova, *et al.*, *Monthly Notices of the Royal Astronomical Society* **526**, 4814 (2023).
- [44] M. Katz, N. Karesis, and N. Korsakova, mikekatz04/eryn: first full release (2023).
- [45] D. Foreman-Mackey, D. W. Hogg, D. Lang, and J. Goodman, *Publications of the Astronomical Society of the Pacific* **125**, 306 (2013), arXiv:1202.3665.
- [46] S. R. Hinton, *The Journal of Open Source Software* **1**, 00045 (2016).

- [47] <https://github.com/esa/lisa-orbit-files>.
- [48] J.-B. Bayle, A. Hees, M. Lilley, *et al.*, Lisa orbits (2025).
- [49] Publicly available at <https://gitlab.in2p3.fr/qbaghi/backgrounds>.
- [50] Publicly available at <https://github.com/mikekatz04/Eryn>.
- [51] S. Babak, M. Hewitson, and A. Petiteau, Lisa sensitivity and snr calculations (2021), arXiv:2108.01167 [astro-ph.IM].
- [52] B. Priestley, *Spectral analysis and time series* (Academic Press, 1982).
- [53] H. E. Krogstad, Journal of Time Series Analysis **3**, 195 (1982).
- [54] L. Isserlis, Biometrika **12**, 134 (1918).
- [55] D. J. Thomson, The Bell System Technical Journal **56**, 1769 (1977).